JACS
JOURNAL OF THE AMERICAN CHEMICAL SOCIETY
Article
pubs.acs.org/JACS

Decoding the Superlattice and Interface Structure of Truncate PbS Nanocrystal-Assembled Supercrystal and Associated Interaction Forces

Ruipeng Li,[†] Kaifu Bian,[‡] Tobias Hanrath,[‡] William A. Bassett,[§] and Zhongwu Wang*[,†]

[†]Cornell High Energy Synchrotron Source, Wilson Laboratory, [‡]School of Chemical and Biomolecular Engineering, and [§]Department of Earth and Atmospheric Sciences, Cornell University, Ithaca, New York 14853, United States

Supporting Information

ABSTRACT: Large scale three-dimensional supercrystals were grown by controlling evaporation of truncate PbS nanocrystal (NC) dispersed hexane suspensions. Electron microscopy analysis confirmed the nature of single supercrystal with a face-centered cubic (fcc) lattice. Synchrotron small/wide angle scattering (SAXS/WAXS) images from three typical crystallographic projections allowed ultimate reconstruction of shape orientations of NCs at different crystallographic sites. Position exchange of distinctly oriented NCs between crystallographic sites produces two nondegeneration shape-related *pseudo-polymorphs* of superlattice that accordingly reduce symmetry from O_h to C_{4h} and C_{2h} with various facet-to-facet arrangements, respectively. *In situ* SAXS measurements of NC-assembled supercrystal and lead oleate and oleic acid upon pressurization provide additional insights into surface ligand density and the nature of ligand−NC interactions and resulting interface structure. These results allow for feasible evaluation of both NC shape and ligand conformation enabled effects that govern the formation and stability of truncate NC assemblies with various superlattice polymorphs and associated NC−ligand interactions in solvent-mediated assembled processes.

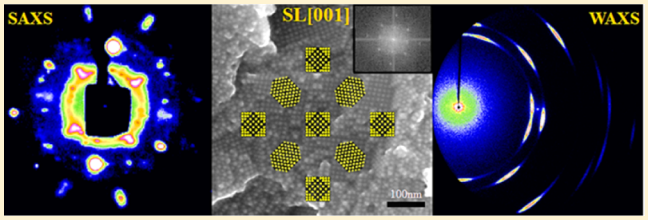

INTRODUCTION

Nanocrystals (NCs) behave like atoms, functionalize with surface-coating organic molecules, interact with judicious solvents, and self-assemble into periodically ordered superlattices.[1−4] These highly ordered NC-based solids, called supercrystal, not only possess or enhance the size- and shape-dependent properties of individual NCs but also yield the novel collective properties from near-field coupling of NC arrays.[5−9] As a consequence, ample opportunities and immense potentials are envisaged toward development of NC-assembled supercrystals as a new type of prototype materials for a broad variety of applications. Recent advances on synthesis and controlled assembly of NCs have been witnessed by fast growth of NC-assembled superlattices, made up of single, binary, and ternary components over control of NC size, shape, and composition.[1−4,6−8,10−22] In parallel, a series of emergent physical properties from assembled superlattices have found applications in optics, electronics, magnetic storage, catalysis, biosensor and imaging.[6−11] However, programmable design and directed fabrication of supercrystals with manipulation of various superlattices for desirable applications are still not enabled because of limited understanding of intricate NC−ligand interactions and complex interplays of multiple driving forces in solvent-mediated NC assembly processes.

NC assemblies involve a variety of interactions and driving forces between inorganic hard NC cores, soft surface-coating molecules, and surrounding solvents.[23−26] Governing interactions and associated driving forces include inter-NC van der Waals attractions, steric repulsions of surface-coating molecules, evaporation-induced capillary forces, attractive depletion forces, surface charge or electric dipole induced Coulomb forces, and entropic forces. In many cases, the simplifying assumption of the NC as a spherical particle fails. Anisotropic interactions emerging from shaped NCs play an additional and critical roles, not only giving rise to directional forces but also enabling novel face-selective functionalization through NC assemblies.[18−21,27] Intricate interactions with various driving forces and environmental perturbations drive NC assembly into very complex superlattice polymorphs.[10,19,27,29,30]

In case of shaped NC assembled supercrystals, one superlattice with defined translation symmetry without consideration of shape aspect could also consist of distinctly oriented NCs at two or more crystallographic sites. If these shaped NCs with different orientations in one given superlattice cell exchange their positions between various crystallographic sites, the shape-related superlattice polymorphs, defined as "*pseudo-polymorph*", are expected to appear accordingly. Apparently, superlattice polymorphs can be recognized differently either in translational symmetry [i.e., traditionally defined superlattice polymorphs, such as the body-centered cubic (bcc), face-centered cubic (fcc), and hexagonal close-packed (hcp) assemblies[4] or in shape orientation (i.e., newly defined pseudo-polymorphs with site-dependent variation of shape orienta-

Received: June 6, 2014
Published: August 6, 2014

   dx.doi.org/10.1021/ja5057032 | J. Am. Chem. Soc. 2014, 136, 12047−12055

tion).[31] These typical superlattice polymorphs or pseudo-polymorphs could functionalize very much like the mostly known structural polymorphs of minerals with various ratios of compositional (or elemental) order/disorder at two crystallographic sites, in which the storage of significant information can be explored and thus used to reconstruct the geological thermal history and structural formation and evolution processes.[32−34] Similarly, insights into typical superlattice (or pseudo-) polymorphs can also be gained and used to trace back how NCs interact with surface-coating molecules, gradually develop from random (or amorphous) into either translational or orientational ordering or both, and ultimately balance multiple interaction forces to form large three-dimensional (3D) supercrystal with thermodynamically favorable superlattice. To accelerate understanding the crystallizing processes of NC supercrystals with a complex diversity of superlattices and thus decoding hidden structural details toward tracing back the NC-assembly processes, it is required to find ways of not only fabricating large 3D single supercrystal but also developing unique and efficient techniques as well. They can be both combined to exploit the supercrystal structure and thus to discover close relations between inorganic NCs and surface-coating ligand molecules at length scales of atom, molecule (or cluster), and nanometer.

PbS NCs not only yield unique electronic properties with potential technological applications but also present ideal building blocks for assemblies with unique translational and orientational ordering. The Bohr exciton radius in PbS is 20 nm, which renders PbS NCs as one of several most strongly quantum confined systems. The energy gap of PbS NCs can be tuned from 0.4 to 2 eV by changing the NC size from 2 to 10 nm.[35−37] Accordingly, their unique tunable properties were exploited in a broad range of technological applications including transistors, photovoltaics, photodetectors, light emitting diodes, and thermoelectrics.[38−48]

Recent works reported dramatic enhancement of direct facet−facet coupling in nanocube arrays and low carrier mobility in disordered spherical NC devices.[19,49−52] These concurrent advances create a compelling motivation to exploit their internal connections that can be used to improve the materials properties and device efficiencies. The simple case should be started with understanding how the shaped NCs interact with surface-coating molecules in solvents to form highly ordered structures that hold great coherence of both NC translational and atomic orientational order with imparting to electronic structures and physical properties of NC assemblies.

Previous studies well documented the size-dependent morphological development of PbS NCs with surface coating of oleic acid (OA) molecules using the hot-injection synthesis approach.[36,37,43,54−59] Upon growth of PbS NCs with particle size from 3 to 15 nm, the shape of NCs develop gradually and follow a growth sequence of sphere, truncate morphology with progressively increased surface facet ratio of {100}/{111} to cube. In this work, we employed truncate PbS NCs with an average size of 11.3 nm and grew large 3D single supercrystals with grain size over several hundred micrometers that have a fcc superlattice and hold full coherence of NC translation and atomic orientation in each individual supercrystal grain.

Using our newly developed unique synchrotron-based small/wide-angle X-ray scattering (SAXS/WAXS) techniques at CHESS,[60,61] the single supercrystal SAXS and WAXS images along several typical crystallographic projections were simultaneously collected from the same volume of the samples. These scattering features allowed us to precisely reconstruct the detailed structure of assembled supercrystal at length scale from atomic to nanoscale. We correlated, for the first time, the position exchange of shaped NCs with distinct orientations between various crystallographic sites and derived the two nondegeneration shape-related superlattice pseudo-polymorphs with reduced symmetry.

To understand how molecular-level interactions between ligands bound to the NC surface influence the formation of pseudo-polymorphs, we further probed the structure of OA and lead oleate [$Pb(OA)_2$]. Combined with *in situ* high-pressure SAXS measurements of NC supercrystals and surface-coating molecules of OA and $Pb(OA)_2$, we provided a primary picture of the NC−ligand interface structure, the packing geometry, and the density of surface ligands embedded inside assembled supercrystals. Moreover, we defined roles of the NC−ligand interaction forces that govern NC assemblies and control structural stabilities of assembled supercrystals. The analyses and insights inform how the complex diversity of driving forces and interactions between NCs and surface ligands guide NC assembly into various superlattices or polymorphs and underscore the critical roles of anisotropic shape and orientation dominated NC−ligand interface structure as well as associated effects.

RESULTS AND DISCUSSIONS

PbS NCs with surface coating of OA molecules were synthesized by the previously developed approach.[37] A typical transmission electron microscopy (TEM) image (Figure 1a)

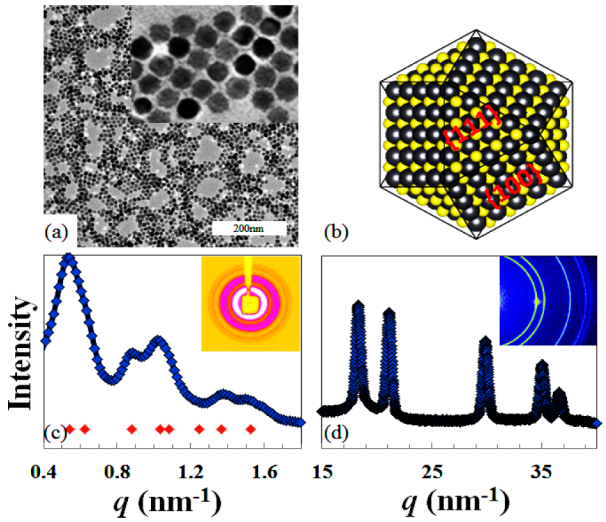

Figure 1. (a) Low- and high-resolution TEM images of PbS nanocrystals (NCs). (b) Schematics of truncate PbS NC with surface termination of eight PbS {111} and six PbS{100} facets. (c) Powder SAXS pattern with inset of 2D image, and diamonds at bottom showing the positions of indexed fcc peaks. (d) Powder WAXS pattern with inset of 2D image. Note: the bright spot on the first WAXS ring of inset (d) is the damage area of the Mar345 detector.

shows that the as-synthesized PbS NCs have an average particle size of 11.3 nm (Figure S1) and display a truncated morphology (inset Figure 1a) with surface termination of six PbS{100} and eight PbS{111} facets (Figure 1b). Controlled evaporation of a colloidal NC suspension of hexane leads NC assembly into periodically ordered superlattice (SL). Powder SAXS pattern indicates that assembled supercrystals have a fcc

dx.doi.org/10.1021/ja5057032 | J. Am. Chem. Soc. 2014, 136, 12047−12055

superlattice with an unit cell parameter of 20.2 nm (Figure 1c); powder WAXS pattern reveals that individual NCs crystallize in a rocksalt-type cubic structure ($Fm3m$) with an atomic lattice constant of 5.942 Å (Figure 1d). However, both the powder SAXS and WAXS patterns do not offer sufficient details to distinguish truncate NCs packing in either a random or an orientational fashion at two crystallographic sites of (0, 0, 0) (corner) and (0.5, 0, 0.5) (face-center) of assembled fcc superlattice.

To explore how truncate PbS NCs align and orient inside fcc superlattice in either a random or an ordered manner with subsequent construction of structural connections from atoms to NCs in mesocrystals in terms of soft ligand bridged interfaces, we gently controlled the evaporation of hexane solvents and grow NCs from hexane solutions into large 3D single supercrystals. A typical scanning electron microscopy (SEM) image reveals that assembled supercrystals have grain size over several hundred microns (Figures 2a and S2).

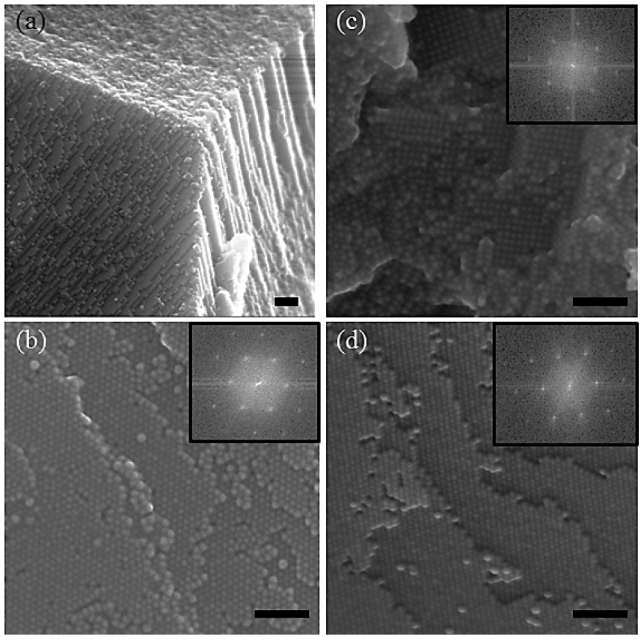

Figure 2. SEM images of PbS NC-assembled single supercrystals at large scale (a) and along projections of SL[111] (b), SL[100] (c), and SL[110] (d). Insets represent their corresponding FFT patterns. The scale bars are 100 nm.

Additional SEM images with higher resolution demonstrate the single-crystal nature of individual supercrystal grains. However, stacking faults were occasionally observed in some supercrystal grains (Figure S3). Fast Fourier transform (FFT) analysis of SEM images (Figure 2b–d) confirms the three typical crystallographic orientations of the fcc superlattice including SL[111], SL[100], and SL[110] directions. SEM and TEM imaging techniques provide convenient and direct images of the superlattice, but they lack enough spatial resolution and in-depth penetration for detailed analysis of the orientational features of truncate NCs in mesoscale supercrystals.

In order to decode the NC translational and atomic orientational details of large NC-assembled fcc supercrystal, high-quality single crystal synchrotron-based SAXS and WAXS images were simultaneously collected from selected single supercrystal grains that display various crystallographic orientations. Figure 3 shows the three typical single crystal

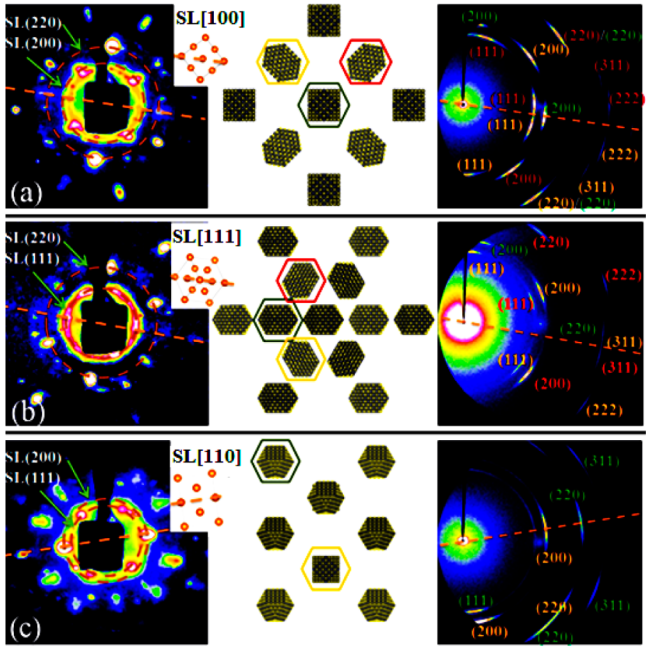

Figure 3. Reconstruction of PbS NC assembled supercrystal with projection of X-rays along SL[100] (a), SL[111] (b), and SL[110] (c). Three panels represent: (left) SAXS images with inset showing the superlattice projection; (middle) structure and orientations of truncate NCs along typical crystallographic direction; and (right) WAXS images with Miller indices. Note: dash lines and circles guide eyes for comparison; various colors represent the differently oriented NCs in superlattice that produce the scattering spots marked in the same colors.

SAXS and WAXS images with projection of X-rays along SL[100], SL[111], and SL[110] direction of the fcc supercrystal, respectively (Figure S4). Handling and transfer of the samples for X-ray illuminations involve damage of fragile supercrystals and attachment of small crystal pieces or powders, accordingly producing additional scattering spots and powder-like arc-shape SAXS features. These SAXS features can be further enhanced by the surface strain of supercrystal grains and slight deviation of NCs from ideal crystallographic sites. To avoid possible confusion of scattering planes between atomic PbS structure and NC-assembled superlattice, PbS(hkl) and SL[hkl] are used to describe the atomic (hkl) plane and superlattice [hkl] projection, respectively. The supercrystal diffracts their atomic planes with X-rays by strict obey of Bragg law in wide angle region. Therefore, the observed WAXS spots are the diffracting X-ray signals from the typical crystalline planes with direct projection on 2D flat detector plane. By correlating the symmetrical features of observed WAXS spots to X-ray projected planes, we can accurately determine how truncate NCs self-arrange anisotropically and distinguish in shape orientation from one to another at various fcc crystallographic sites.

Single crystal SAXS image in Figure 3a reveals typical four-fold symmetrical spots in both SL(200) and SL(220) (marked by dashed circle), confirming the SL[100] orientation along the X-rays. However, WAXS image along the SL[100] orientation consists of a series of scattering spots that cannot be exclusively assigned to only one single group of oriented NCs. If all NCs display identical orientation, then the supercrystal should act as single atom-packed crystal and does not scatter the orientation-forbidden spots. The observed PbS(200) spots display an eight-

dx.doi.org/10.1021/ja5057032 | J. Am. Chem. Soc. 2014, 136, 12047–12055

fold symmetry, indicative of the overlapping of two groups of four-fold symmetrical spots with an in-plane mismatch angle of 45° (see the details in Figure 3 and Table S1). Correlating the typical interplanar angle of 54.7° between PbS(200) and PbS(111), one group of oriented NCs produces the PbS(200) and PbS(111) spots (marked in orange), indicating that the oriented NCs have their PbS(110) planes perpendicular to X-rays and SL[100] as well. Upon rotation of NCs with an in-plane angle of 90°, these NCs (orange) further produce four-fold symmetrical Pb(220) spots (red) and the PbS(311) and PbS(222) spots. Another group of oriented NCs with PbS[100]//SL[100] produces the four-fold symmetrical Pb(200) spots (green) that display an in-plane mismatch angle of 45°. It can be thus concluded that the SL[100] projected planes consist of two groups of oriented NCs in which PbS[100] and PbS[110] are parallel to SL[100], respectively. Figure S5b presents the angular plot of PbS(200) scattering ring, revealing that both the orange and red spots have approximately equivalent intensity, but they are apparently much weaker than the green ones. One fcc superlattice unit cell consists of four NCs: (1) three NCs at face-centers and (2) one NC at corner. Two face-center NCs (red and orange) produce the four-fold symmetrical PbS(200) spots, but the third one remains uncertain. If the third NC orients as same as the corner NCs (marked as "peak2" in PbS[100] orientation in Figure S5), PbS[100]-oriented NCs should scatter X-rays with intensity twice of that from PbS[110]-oriented NCs. As shown in Table S1, the green one was calculated with intensity as large as twice in height and 1.43 times in area to that of the red and orange one, in fair agreement with the scattering intensity of double-numbered NCs (see Figure S5b,c). Therefore, we can conclude that the third NC at face center has the same orientation as the NC at corner.

Figure 3b shows the SAXS and WAXS images of single supercrystal with projection of X-rays along the SL[111] direction. Both SL(111) and SL(220) in SAXS image (Figure 3b, left) display a typical six-fold symmetrical spotty feature, but no SL(200) appears. These scattering signatures indicate the orientation of SL[111] parallel to X-rays. In principle, X-ray scatterings from SL(111) planes are forbidden upon preferred alignment of SL[111] parallel to X-rays. In comparison with atomic crystal that interacts X-rays with straightforward obedience of the Bragg law in a wide angle region, the supercrystal comprised of considerably enlarged NC building blocks diffracts X-rays only at much smaller angles (i.e., $2\theta < 5°$). Small deviation of NCs from ideal crystallographic sites can give rise to the orientation-forbidden spots. Therefore, it is understandable to observe one set of weak SL(111) spots. If we look at the powder supercrystal samples that lack orientation, the SL(111) peak is at least 10 times more intense than the SL(220) peak (Figures 1c and S4). To facilitate the comparison of observed symmetrical features (Figure S6a), we added a dashed line as a reference to present the horizon of the superlattice in SAXS/WAXS images and insets. As the PbS(200) and PbS(220) spots reach a mismatch angle of 30° (Figure S6b), they both consist of the typical six-fold symmetrical spots. Collectively, the shape orientations of NCs along the SL[111] direction can be reconstructed as follows (Figure S6c): (1) three NCs at face center form a three-fold symmetry, and (2) their PbS(110) planes are parallel to SL[111], in agreement with the observed six-fold symmetrical spots of PbS(220) and PbS(111). If NC shape is considered as one additional constraint, the three-fold axis vanishes and instead a new 2_1 symmetry arises. The above analyses also explain well the observed symmetrical features in PbS(111), PbS(311), and PbS(222) rings.

We now turn to describe the orientation of NCs in the corner sites of the superlattice. If NCs at corners were oriented in the same direction as NCs at face centers, the lattice reduces from four-fold symmetry (C_{4h}) to two-fold symmetry (C_{2h}). However, our analysis suggests that this is not the case. SAXS and WAXS images collected along the SL[110] projection (Figure 3c: left and right) offer insights to reconstruct the shape orientations of NCs at corner sites. Based on the previous description of superlattice structure, SL[110] projected plane consists of two groups of oriented NCs with PbS[100] and PbS[$11\sqrt{2}$] parallel to SL[110]. Note: PbS[$11\sqrt{2}$] is defined and shown in Figure S7. The first group of NCs with PbS[100]//SL[110] (orange in Figure 3c, middle) produces the four-fold symmetrical PbS(200) spots. The second group of oriented NCs with PbS[$11\sqrt{2}$]//SL[110] produces only the PbS(220) spots along the horizon line in Figure 3a (left). As shown in Figure S7, the orange spots sited at a rotation angle of 45° from the dashed line are produced from the first group of NCs, and the green spots with six-fold symmetrical feature from the second group of NCs. Simulation of single supercrystal WAXS patterns (Figure S7d–f) confirmed the reliability of the above structure reconstruction and also explained the appearance of orientation-forbidden WAXS peaks.

In principle, the second group of NCs with PbS[$11\sqrt{2}$]// SL[110] (green) should not have any contribution to either one of the observed PbS(111), PbS(311), and PbS(220) spots. However, azimuthal integrations of SL[110] orientation-related WAXS peaks revealed a powder-like arc-shape scattering feature in which the angular width of scattering spots is as large as 30°. These scattering signatures indicate significant lattice distortion and positional deviation of NCs along the SL[110] direction. The lattice distortion and positional deviation break down the lattice symmetry, accordingly giving rise to the PbS[111]- and/or PbS[112]-related scattering spots. Theoretical simulations further reveal the births of both the six-fold symmetrical PbS (220) spots from PbS[111]-oriented NCs (Figure S7d) and the rectangular distributed spots of PbS(311) and PbS(111) spots from PbS[112]-oriented NCs (Figure S7f). The observed lattice distortion of NCs with 9.7° misorientation of PbS[$11\sqrt{2}$] to both PbS[111] and PbS[112] provides reasonable interpretation for the unfavorable appearance of orientation-forbidden spots of PbS(111) and PbS(311) scatterings.

Careful analyses of single crystal SAXS and WAXS and HRSEM images allowed us to create a detailed reconstruction of NC translation and atomic orientation of the supercrystal at atomic to nanometric level. To go beyond describing the observed structure, we sought to understand the underlying formation mechanism. In particular, we aimed at understanding the role of molecular level interactions between soft ligands bound to the hard inorganic NC core. Based on the same sets of SAXS and WAXS images, the shape-related pseudo-polymorphs could arise from the exchange of positions of truncated NCs between three face-center sites in one fcc superlattice cell.[31] As a consequence, six shape-related superlattice pseudo-polymorphs were derived and then merged into two nondegeneration superlattice pseudo-polymorphs according to the superlattice transformation, which are shown in Figure 4. More details about the polymorphic degeneration and

dx.doi.org/10.1021/ja5057032 | J. Am. Chem. Soc. 2014, 136, 12047−12055

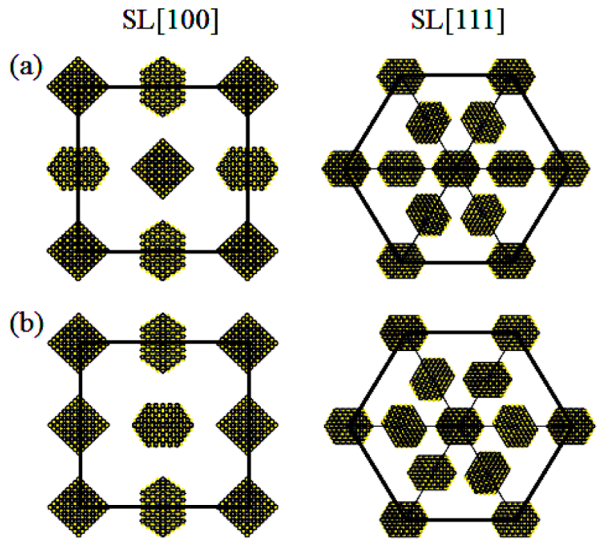

Figure 4. Two nondegeneration shape-related pseudo-polymorphs derived from the basic fcc superlattice of truncate NC assembled supercrystals that produce identical sets of single crystal SAXS and WAXS images given in Figure 3. Projections along SL[100] and SL[111] show the various orientations of truncated NCs between two pseudo-polymorphs. Insets (a) and (b) include a C_{4h} and C_{2h} symmetry, respectively.

their superlattice transformation correlations are given in Figure S8. These shape-related superlattice pseudo-polymorphs produce identical sets of single crystal SAXS and WAXS patterns as shown in Figure 3. Adding NC shape as one constraint in lattice determination, NCs at corners include only one mirror symmetry along the SL[111] projection. Applying similar analysis to the NCs at face-center sites, high symmetry superlattice (O_h) breaks down. Accordingly, the original fcc superlattice transforms into two lower symmetry superlattice pseudo-polymorphs (Figure 4): (1) one at top includes a C_{4h} symmetry; and (2) one at the bottom includes a C_{2h} symmetry. These two superlattice pseudo-polymorphs are also different in both number of facet−facet interacting arrangements and type of shape orientation of NCs between the corner and face-center sites.

To gain new insight into the facet-specific interactions between shaped PbS NCs, we therefore turn to understand the detailed nature of the surface structure and associated facet-to-facet arrangements of neighboring PbS NCs in the superlattice. The structure of truncate PbS NC building blocks can be reconstructed at surfaces with eight triangle PbS{111} and six square PbS{100} facets (Figure 1b). Each NC in fcc superlattice is surrounded by 12 nearest neighbors to achieve the highest packing density. Since each NC has only 12 surface facets capable of contacting directly with surface facets of neighboring NCs, only three types of direct facet-to-facet contacts are allowed. These facet−facet interactions include {100}-to-{100}, {100}-to-{111} and {111}-to-{111} configurations. One fcc superlattice unit cell consists of 4 truncate NCs and involves 24 direct facet-to-facet contacts. Details of these direct facet-to-facet contacts in two nondegeneration shape-related superlattice pseudo-polymorphs are estimated and summarized in Tables S2 and S3.

Analysis of facet-specific interactions between proximate NCs offers important clues to the energetic of different pseudo-polymorphs. PbS{111} facets are characterized with higher surface atomic area density than PbS{100} facets, so increase of the number of {111}-to-{111} contacts in one unit cell are highly favored toward enhancing the NC-NC interactions. The first superlattice pseudo-polymorph (Figure 4a, Tables S2 and S3) consists of higher number of {111}-to-{111} contacts. Under the assumption of the molecular ligands in alignment with the orientation of the NC facet, this NC arrangement not only enlarges the surface ligand area packing density to effectively enhance the steric force interactions but also maximizes the molecular configurational entropy to improve the structural stability. The model in Figure 5 reveals how to

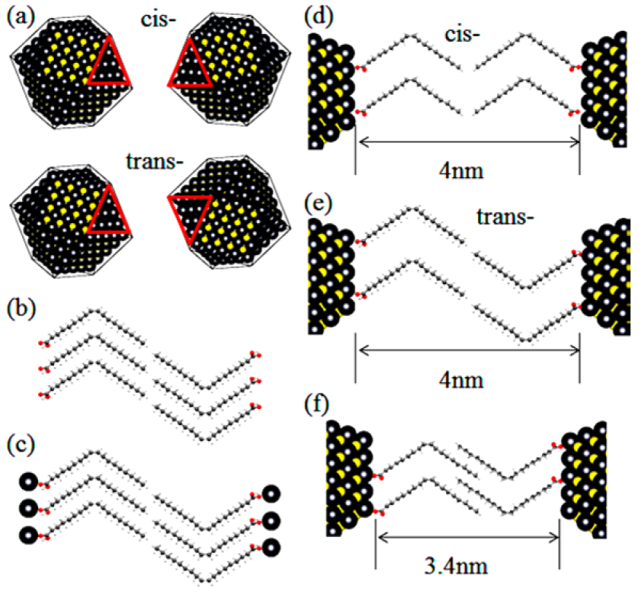

Figure 5. Schematics of inter-NC packing geometries: (a) *cis*- (top) and *trans*-geometry (bottom) between two interacting PbS{111} surface facets. Demonstrations of OA interactions in (b) pure OA crystal, (c) $Pb(OA)_2$ crystal and (d−f) OAs inside NC supercrystal with various local structures in (d) *cis*-, (e and f) *trans*-geometry.

account for the local packing structure of surface molecules. PbS{111} facets from two neighboring NCs can be arranged in either a *trans*- or a *cis*-geometry. These two distinct structural geometries are both capable of increasing the ordering ratio and packing density of surface ligands and accordingly strengthen the ligand−ligand interactions. As shown in Figure 5, the *trans*-geometrical packing of NCs facilitates intercalation of ligand chains from two neighboring NCs. By contrast, the *cis*-geometrical packing can increase ligand conformational entropy. Comparatively, the first superlattice pseudo-polymorph (Figure 4a, Tables S2 and S3) holds advantages with not only a higher lattice symmetry for enhancing structural stability but also a ligand-favorable *cis*-geometry for maximizing the ligand conformational entropy. While the *trans*-geometry-enabled increases in both ordering ratio and intercalation capability of ligand molecules are able to stabilize the structure of assembled supercrystals, the *cis*-geometry-induced increase in conformational entropy plays a more critical role in solvent-mediated NC assembly process.

Previous reports of PbS NC-assembled fcc superlattice thin films did not observe orientational ordering. The fcc supercrystals analyzed in this work show significant orientational ordering which underscores the interplay of thermodynamic and kinetic factors of superlattice formation. The superlattices

dx.doi.org/10.1021/ja5057032 | J. Am. Chem. Soc. 2014, 136, 12047−12055

assembled in this work were formed at a much slower rate than previously studied self-assembly of superlattices in thin films. It can be therefore concluded that, if NC assembly process is reasonably controlled to maintain a thermodynamic equilibrium state, the first shape-related pseudo-polymorph of superlattice (Figure 4a) prefers to form and dominate the structure of assembled supercrystals.

The structures of OA and $Pb(OA)_2$ molecules were also explored and systematically analyzed to understand more about the ligand−ligand interactions and the interface structure between neighboring NCs in assembled supercrystals. At ambient conditions, OA molecules appear as amorphous liquid without long-range order. Cooling or pressurizing of OAs transforms liquid to a lamellar crystalline phase with structure in either one of α, β, and γ polymorphs.[62−64] OA molecules are arranged in α and γ polymorphs with a *trans*-geometry. These two structure polymorphs are similar, but they display slight difference of tilt angle along the *c*-axis. A relatively larger OA tilt angle in α phase leads to a smaller lamellar distance of 4.0 nm than the lamellar distance of 4.3 nm in γ phase. However, a dramatic change appears in β phase in which neighboring OAs aligned in parallel within a monolayer are packed in an alternating way, accordingly reducing the lamellar distance to ∼3.5 nm. Similar analysis was applied to probe the structure of lead oleate [$Pb(OA)_2$]. Bonding one Pb atom with two OA molecules forms one long $Pb(OA)_2$ chain, and similarly, these long chain molecules also crystallize in a lamellar structure phase that has an enlarged lamellar distance of 4.65 nm.[4]

Previous studies demonstrated that OA molecules are bound to Pb sites at NC surfaces, so the structural similarity between surface-coating OAs and single β phase can be excluded.[4,62] Figure 5b,c shows cartoon schematics of crystalline OA in α form and $Pb(OA)_2$ phase, respectively. SAXS measurements of PbS NC supercrystal indicate that the inter-NC distance falls into a narrow range of 3.0−3.4 nm, smaller than the lamellar distances of 4.0 and 4.65 nm observed in pure OA (α form) and $Pb(OA)_2$ crystalline phase, respectively. Therefore, OAs could be packed at NC−NC interfaces inside supercrystal in several possible ways (Figure 5): (1) amorphous jamming; (2) *cis*-geometry; and (3) *trans*-geometry. By correlating the OA molecule length of ∼2 nm, if OAs are packed in *cis*-geometry (Figure 5d), the inter-NC distance should be more or less about 4 nm, equivalent to double the OA length. Based on the measured inter-NC distance of 3.0−3.4 nm from assembled supercrystals, it is expected that the surface-coating OAs from neighboring NCs intercalate each other and develop an ordered local structure to enhance the ligand−ligand interactions (Figure 5f).

To understand how the surface ligand intercalations and the packing structure of OAs were developed inside NC supercrystal, *in situ* SAXS measurements were performed on NC supercrystal and pure $Pb(OA)_2$ and OA under pressures. Figure 6 shows the pressure-dependent changes of both the inter-NC distance of assembled supercrystal and the lamellar distances of $Pb(OA)_2$ and OA solids. Upon compression of three samples from 0 to ∼6 GPa, both $Pb(OA)_2$ and OA phases display a similar reducing magnitude of lamellar spacing on the order of ∼1 Å, but NC supercrystals reduce inter-NC distance on a much greater order of 1.22 nm. The pronounced difference in compression behaviors between the three samples suggests a significantly lower packing density of OAs in assembled supercrystal than these in ordered pure $Pb(OA)_2$ and OA crystal phases (Figure 6). Since OA molecules prefer to be

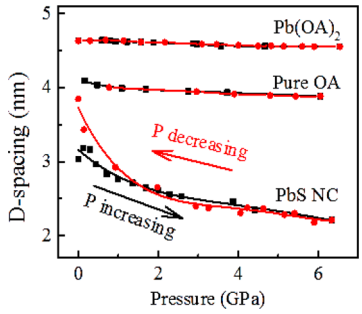

Figure 6. Inter-NC distance of PbS NC assembled supercrystal and the observed lamellar distances of OA and $Pb(OA)_2$ solids as a function of pressure.

bound at Pb sites at NC surfaces,[65,66] if all Pb sites at NC surfaces are bound by OA molecules, then the area packing densities of OAs at {111} and {100} surface facets are estimated to be about 6.55 and 5.68 OA/nm^2, respectively (see the detailed calculations in SI). They are apparently greater than the area packing density of 4.4 OA/nm^2 calculated from the highly ordered pure crystalline OA and $Pb(OA)_2$ phase. If NC surface facets have such a unfavorable higher OA packing density than or a reasonable density equivalent to that of the pure OA and $Pb(OA)_2$ phases, NC supercrystals should behave like the lamellar OA and $Pb(OA)_2$ phase and display a higher or at least a close pressure-dependent incompressibility, rather a fast reduction of inter-NC distance observed in NC supercrystal. To allow such a quick pressure-dependent reduction of inter-NC distance, at least half of Pb sites at NC surfaces are not bound by OA molecule so that enough room remains for feasible intercalation of surface OAs from neighboring NCs.

Figure 7 shows two binding models of OAs at two surface facets of PbS{100} and PbS{111}: (1) two head oxygen atoms of one OA chain are linked to two Pb sites (Figure 7, top) and no bare Pb site is exposed at NC surfaces; and (2) each OA chain has only one head oxygen atom being linked with Pb site,

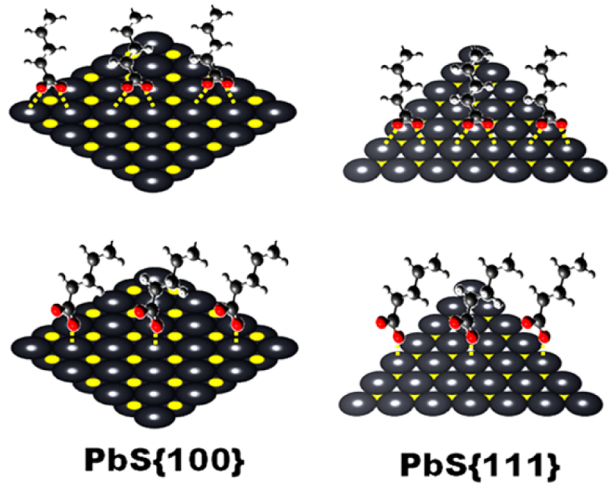

Figure 7. Demonstration of the OA binding models at two surface facets of PbS{100} and PbS{111} that allow intercalation of OA molecules. There are two OA binding models: (1) one at top panel with two head oxygen atoms bound to two Pb sites, and no bare Pb exposed at surfaces; and (2) the other one at bottom with one head oxygen atom bound to one Pb site, and half Pb sites are required to remain barely exposed at surfaces.

dx.doi.org/10.1021/ja5057032 | J. Am. Chem. Soc. 2014, 136, 12047−12055

and half Pb sites are barely exposed at NC surfaces (Figure 7, bottom). Similar to the bonding of one Pb atom to two oxygen atoms in $Pb(OA)_2$, the double-binding model makes the OA-binding at NC surfaces more stable than the single-binding model does. Previous studies reveal that the air-induced loss of surface-coating OAs most likely takes place at PbS{100} surfaces,[67] and instead PbS{111}-terminated NCs appear to be air-stable. Therefore, it can be concluded that PbS{111} surfaces favor a double-site OA binding, and PbS{100} surfaces favor a single-site OA binding. Both the PbS{111}- and PbS{100}-terminated surfaces have an area density of Pb sites greater than the theoretical density of 4.4 OA/nm^2, so the average OA density at NC surfaces can be reasonably estimated based on the assumption that 1/3−1/2 Pb sites at surfaces are bound by OAs (see the details in SI). Accordingly, the OA packing density can be estimated in a reasonable range of 2.04−3.06 OA/nm^2 (Table S4), in fair agreement with theoretical and experimental area packing densities of OAs coated at NC surfaces of PbS and PbSe.[65−69] The above reconstructed superlattice pseudo-polymorphs and estimated packing densities suggest that OAs at NC interfaces can be developed in either a *trans*- or a *cis*-geometry to effectively increase the magnitude of OA intercalations, which accordingly strengthens the ligand−ligand interactions and maximizes the structural stability.

Decompression of supercrystals from high pressure to ambient conditions does not return inter-NC distance to the initial value of 3.4 nm. Instead the spacing expands to a slight larger distance of 3.8 nm which is still shorter than the double OA length of 4.0 nm (Figure 6). In NC assemblies, multiple interactions between NCs and ligands and solvents cause formation of the stable fcc superlattice in which the interaction forces between NCs and ligands can be considered to eventually achieve an equilibrium state at a critical NC−NC separation distance. The ligand−ligand interactions are purely repulsive in the presence of good solvents,[70] so it is reasonable to assume that the van der Waals attraction forces between NCs balance the ligand−ligand repulsive forces in finally assembled supercrystal. With this assumption, the inter-NC distance after complete release of pressure should return to the original equilibrium distance, rather than an observed enlargement of inter-NC distance. Explaining this unexpected observation requires consideration of the drying-induced effect during the self-assembly process of the supercrystal. The drying-induced contraction of supercrystal grains slightly shortens the inter-NC distance, and simultaneously the ligand bundles give rise to strong ligand−ligand attractive forces in completely dried supercrystals. Upon compression of supercrystals in DAC and associated reduction of inter-NC distance, an elastic contribution arises and quickly exceeds thermal energy and thus dominates the ligand−ligand interactions. Importantly, application of external forces can break the weak side-to-side bonding of ligand bundles and accordingly free up the ligand molecules and increase molecular conformational entropy. After entire release of pressure, elastic forces stored in ligand bundles drive the squeezed molecule chains bouncing back to the starting equilibrium inter-NC distance. Because of the pressure-induced "debonding" and weakening of ligand−ligand interactions, it is expected to yield a slightly larger inter-NC distance. The above analysis reasonably explains the enlarged inter-NC distance of 3.8 nm of recovered samples, rather than a return to the starting spacing of 3.4 nm before compression.

Detailed reconstruction of truncate PbS NC assembled supercrystal with shape-related superlattice pseudo-polymorphs and thorough structural analyses of surface-coating molecules allows us to draw a primary picture of how NC assemblies take advantage of NC shape anisotropy and molecular conformation at NC surfaces to expand the superlattice phase diagram and increase the structural complexity and functionality of NC−ligand interacted assembles (Scheme 1). At the most basic level,

Scheme 1. Development of NC Assembled Superlattice Complexities upon Coordination of NC Shape Anisotropy and Conformational Freedom of Surface-Coating Molecules

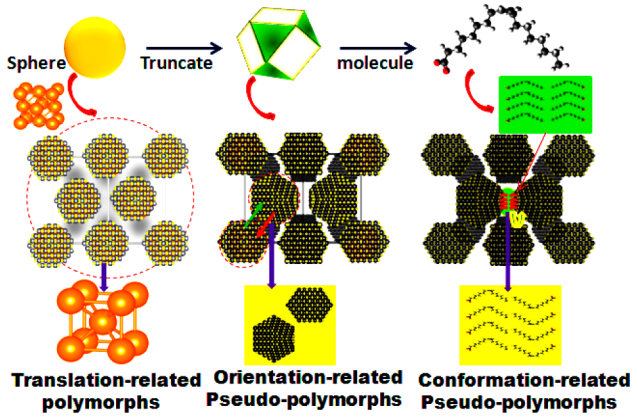

spherical NCs can be simply described as atoms and favor primary packing into a fcc superlattice that has the highest packing density of 74% (left, Scheme 1).[1,2] Upon environmental perturbation of either temperature or pressure or both, the fcc-packed supercrystal transforms to various superlattice polymorphs, referred as to the traditionally defined translation-related "structure polymorph", such as hcp and bcc superlattice with a packing density close to and smaller than fcc, respectively.[4] When NCs develop in shape and become nonspherical, strong anisotropic effects appear and drive NC assembly into much complex diversity of superlattices.[10−22] For example, NC assemblies have identical translation symmetry of fcc, but NCs orient differently at corner and face-center sites (middle, Scheme 1), accordingly giving rise to a series of shape-related superlattice pseudo-polymorphs,[31] such as the two shape-related superlattice pseudo-polymorphs derived in this work. In addition, NC surfaces are not naked and are always passivated by organic molecules. These molecules prevent NCs from aggregation and growth and also enable dissolving of NCs in solvents for additional physical processing. Once while NCs interact with surface ligand molecules and surrounding solvents to form NC supercrystal, surface molecules can also develop local structures with distinct conformations to bridge NCs together.[71−77] The conformational arrangements of surface molecules can develop in various structure forms, such as random (disordered), *cis*- and *trans*-configuration (right, Scheme 1). Given one shape-related superlattice pseudo-polymorph, the conformational variation of surface molecules can further generate a series of conformation-related superlattice pseudo-polymorphs. This simple structural progression of both NCs and ligand molecules from translation to anisotropic shape and ultimately to molecular conformation allows to form a large increase in the number of superlattice polymorphs. The developments of these superlattice polymorphs are simultaneously accompanied by significant

dx.doi.org/10.1021/ja5057032 | J. Am. Chem. Soc. 2014, 136, 12047−12055

symmetry reduction, structural enhancement, and increased functional complexity. In this study, we combined the fabrication of large single supercrystal and the development of synchrotron-based single crystal SAXS/WAXS technique and walked one significant step to uncover the mysteries of assembled superlattices and complex pseudo-polymorphs. Upon development of novel and powerful approaches, such as synchrotron-based scattering and spectroscopic techniques, we will be able to provide a much clearer image about the superlattice phase diagrams and functionalities of NC assemblies upon change of the size, shape, composition, and surface molecular decoration of NC building block.[78−81]

CONCLUSIONS

Controlled evaporation of truncate PbS NC-dispersed solutions at slower rate allowed successful growth of large scale 3D single crystal supercrystals that have a fcc superlattice. Electron microscopy imaging characterized the full coherence of NC translation and atomic orientation of individual supercrystal grains. Single crystal SAXS and WAXS patterns collected from projection of X-rays along SL[111], SL[110], and SL[100] direction allowed us to precisely reconstruct how truncated PbS NCs orient anisotropically and occupy different crystallographic sites to form highly ordered fcc supercrystal. Coordination of NC shape orientation in lattice analysis of the same sets of single supercrystal SAXS and WAXS images gives rise to two nondegeneration shape-related superlattice pseudo-polymorphs in which the lattice symmetry reduces from O_h to C_{4h} and C_{2h}, respectively. The superlattice pseudo-polymorph, which holds a C_{4h} symmetry and maximizes the {111}-to-{111} contacts, represents the most favorable low-energy superlattice of assembled supercrystals if the assembly process maintains a thermodynamic equilibrium. The area density of OAs at NC surfaces was estimated in the range of 2.04−3.06 OA/nm^2. Combined with NC translation and anisotropic shape orientation as well as surface ligand conformation, our detailed structural reconstruction and analyses provide a significant advance in understanding the superlattice phase diagram with extended diversity of superlattice polymorphs and complicated functionalities.

ASSOCIATED CONTENT

Supporting Information

Additional data include experimental details, calculation methods on packing density and inter-NP distance, tables, additional SEM images, and SAXS patterns. This material is available free of charge via the Internet at http://pubs.acs.org.

AUTHOR INFORMATION

Corresponding Author

zw42@cornell.edu

Notes

The authors declare no competing financial interest.

ACKNOWLEDGMENTS

We appreciate technical assistance from all CHESS staff at Cornell University. CHESS is supported by the NSF awards DMR-0936384 and DMR-1332208. K.B. is supported by the NSF award DMR-1056943.

REFERENCES

(1) Murray, C. B.; Kagan, C. R.; Bawendi, M. G. *Annu. Rev. Mater. Sci.* **2000**, *30*, 545−610.
(2) Murray, C. B.; Kagan, C. R.; Bawendi, M. G. *Science* **1995**, *270*, 1335−1338.
(3) Macfarlane, R. J.; Lee, B.; Jones, M. R.; Harris, N.; Schatz, G. C.; Mirkin, C. A. *Science* **2011**, *334*, 204−208.
(4) Wang, Z. W.; Schliehe, C.; Bian, K.; Dale, D.; Bassett, W. A.; Hanrath, T.; Klinke, C.; Weller, H. *Nano Lett.* **2013**, *13*, 1303−1311.
(5) Collier, C. P.; Saykally, R. J.; Shiang, J. J.; Henrichs, S. E.; Heath, J. R. *Science* **1997**, *277*, 1978−1981.
(6) Talapin, D. V.; Lee, J. S.; Kavalenko, M. V.; Shevchenko, E. V. *Chem. Rev.* **2010**, *110*, 389−458.
(7) Courty, A.; Mermet, A.; Albouy, P. A.; Duval, E.; Pileni, M. P. *Nat. Mater.* **2005**, *2*, 395−398.
(8) Nie, Z.; Petukhova, A.; Kumacheva, E. *Nat. Nanotechnol.* **2010**, *5*, 15−25.
(9) Su, K. H.; Wei, Q. H.; Zhang, X.; Mock, J. J.; Smith, D. R.; Schultz, S. *Nano Lett.* **2003**, *3*, 1087−1090.
(10) Wang, T.; Zhuang, J.; Lynch, J.; Wang, Z.; Wang, X.; LaMontagne, D.; Wu, H.; Wang, Z.; Cao, Y. C. *Science* **2012**, *338*, 358−363.
(11) Ye, X.; Collins, J. E.; Kang, Y.; Chen, J.; Chen, D. T. N.; Yodh, A. G.; Murray, C. B. *Proc. Natl. Acad. Sci. U.S.A.* **2010**, *107*, 22430−22435.
(12) Jones, M. R.; Macfarlane, R. J.; Lee, B.; Zhang, J.; Young, K. L.; Senesi, A. J.; Mirkin, C. A. *Nat. Mater.* **2010**, *9*, 913−917.
(13) Macfarlane, R. J.; Jones, M. R.; Lee, B.; Auyeung, E.; Mirkin, C. A. *Science* **2013**, *341*, 1222−5.
(14) Shevchenko, E. V.; Talapin, D. V.; Kotov, N. A.; O'Brien, S.; Murray, C. B. *Nature* **2006**, *439*, 55−59.
(15) Stebe, S. J.; Lewandowski, E.; Ghosh, M. *Science* **2009**, *325*, 159−160.
(16) Dong, A. G.; Ye, X. C.; Chen, J.; Murray, C. B. *Nano Lett.* **2001**, *11*, 1804−1809.
(17) Ye, X. C.; Chen, J.; Murray, C. B. *J. Am. Chem. Soc.* **2011**, *133*, 2613−2620.
(18) Damasceno, P. F.; Engel, M.; Glotzer, S. C. *Science* **2012**, *337*, 453−457.
(19) Quan, Z.; Fang, J. *Nano Today* **2010**, *5*, 390.
(20) Henzie, J.; Grünwald, M.; Widmer-Cooper, A.; Geissler, P. L.; Yang, P. *Nat. Mater.* **2011**, *11*, 131.
(21) Miszta, K.; Graaf, J. D.; Bertoni, G.; Dorfs, D.; Brescia, R.; Marras, S.; Ceseracciu, L.; Cingolani, R.; Dijkstra, M.; Manna, L. *Nat. Mater.* **2011**, *10*, 872−876.
(22) Smith, D. K.; Goodfellow, B.; Smilgies, D.-M.; Korgel, B. A. *J. Am. Chem. Soc.* **2009**, *131*, 3281−3290.
(23) Bishop, K. J. M.; Wilmer, C. E.; Soh, S.; Grzybowski, B. A. *Small* **2009**, *5*, 1600−1630.
(24) Mann, S. *Nat. Mater.* **2009**, *9*, 891−792.
(25) Min, Y.; Akbulut, M.; Kristiansen, K.; Golan, Y.; Israelachvili, J. *Nat. Mater.* **2008**, *7*, 827−838.
(26) Talapin, D. V. *ACS Nano* **2008**, *3*, 1097−1100.
(27) Glotzer, S. C.; Solomon, M. J. *Nat. Mater.* **2007**, *6*, 557−562.
(28) Ye, X.; Chen, J.; Engel, M.; Millan, J. A.; Li, W.; Qi, L.; Xing, G. Z.; Collins, J. E.; Kagan, C. R.; Li, J.; Glotzer, S. C.; Murray, C. B. *Nat. Chem.* **2013**, *5*, 466−473.
(29) Quan, Z.; Xu, H.; Wang, C.; Wen, X.; Wang, Y.; Zhu, J.; Li, R.; Sheehan, C.; Wang, Z.; Smilgies, D. M.; Luo, Z.; Fang, J. *J. Am. Chem. Soc.* **2014**, *136*, 1352−1359.
(30) Wang, T.; Wang, X.; LaMontagne, D.; Wang, Z.; Wang, Z. W.; Cao, Y. C. *J. Am. Chem. Soc.* **2012**, *134*, 18225−18228.
(31) Simon, P.; Rosseeva, E.; Baburin, I. A.; Liebscher, L.; Hickey, S. G.; Cardoso-Gil, R.; Eychumuller, A.; Kniep, R.; Carrillo-Cabrera, C. *Angew. Chem., Int. Ed.* **2012**, *51*, 10776−10781.
(32) Dyar, M. D.; McGuire, A. V.; Harrell, M. D. *Geochim. Cosmochim. Acta* **1992**, *56*, 2579−2586.
(33) Molin, G. M.; Saxena, S. K.; Brizi, E. *Earth Planet. Sci. Lett.* **1991**, *105*, 260−265.

(34) Saxena, S. K.; Dal Negro, A. *Bull. Mineral.* **1983**, *106*, 443−449.
(35) Wise, F. W. *Acc. Chem. Res.* **2000**, *23*, 773−780.
(36) Cademartiri, L.; Montanari, E.; Calestani, G.; Migliori, A.; Guagliardi, A.; Ozin, G. A. *J. Am. Chem. Soc.* **2006**, *128*, 10337−10346.
(37) Hines, M. A.; Sholes, G. D. *Adv. Mater.* **2003**, *15*, 1844−1849.
(38) McDonald, S. A.; Konstantatos, C.; Zhang, S.; Cyr, P. W.; Klem, E. J. D.; Levina, L.; Sargent, E. H. *Nat. Mater.* **2005**, *4*, 138−142.
(39) Rauch, T.; Boberl, M.; Tedde, S. F.; Furst, J.; Kovalenko, M.V.; Hesser, G.; Lemmer, U.; Heiss, W.; Hayden, O. *Nat. Photonics* **2009**, *3*, 332−336.
(40) Hanrath, T. *J. Vac. Sci. Technol., A* **2012**, *30*, 030802.
(41) Bisri, S. Z.; Piliego, C.; Yarema, M.; Heiss, W.; Loi, M. A. *Adv. Mater.* **2013**, *25*, 4309−4314.
(42) Gao, J.; Perkins, C. L.; Luther, J. M.; Hanna, M. C.; Chen, H. Y.; Semonin, O. E.; Nozik, A. J.; Ellingson, R. J.; Beard, M. C. *Nano Lett.* **2011**, *11*, 3263−3266.
(43) Etgar, L.; Moehl, T.; Gabriel, S.; Hickey, S. G.; Eychmuller, A.; Gratzel, M. *ACS Nano* **2012**, *6*, 3092−3099.
(44) Tang, J.; Sargent, E. H. *Adv. Mater.* **2010**, *23*, 12−29.
(45) Konstantatos, G.; Howard, I.; Fischer, A.; Hoogland, S.; Clifford, J.; Klem, E.; Levina, L.; Sargent, E. *Nature* **2006**, *442*, 180−183.
(46) Sun, L.; Choi, J. J.; Stachnik, D.; Bartnik, A. C.; Hyun, B. R.; Malliaras, G. G.; Hanrath, T.; Wise, F. W. *Nat. Nanotechnol.* **2012**, *7*, 369−373.
(47) Ma, X.; Xu, F.; Benavides, J.; Cloutier, S. G. *Org. Electronics* **2012**, *13*, 525−531.
(48) Ibáñez, M.; Zamani, R.; Gorsse, S.; Fan, J.; Ortega, S.; Cadavid, D.; Morante, J. R.; Arbiol, J.; Cabot, A. *ACS Nano* **2013**, *7*, 2573−2586.
(49) Polarz, S. *Adv. Funct. Mater.* **2011**, *21*, 3214−3230.
(50) Lapointe, C. P.; Mason, T. G.; Smalyukh, I. I. *Science* **2009**, *326*, 1083−1086.
(51) Liljeroth, P.; Overgaag, K.; Urbieta, A.; Grandidier, B.; Hickey, S. G.; Vanmaekelbergh, D. *Phys. Rev. Lett.* **2006**, *97*, 096803.
(52) Koh, W.-k.; Saudari, S. R.; Fafarman, A. T.; Kagan, C. R.; Murray, C. B. *Nano Lett.* **2011**, *11*, 4764−4767.
(53) Quan, Z.; Li, C.; Zhang, X.; Yang, J.; Yang, P.; Zhang, C.; Lin, J. *Cryst. Growth Des.* **2008**, *8*, 2387−2392.
(54) Wang, Y.; Tang, A.; Li, K.; Yang, C.; Wang, M.; Ye, H.; Hou, Y.; Teng, F. *Langmuir* **2012**, *28*, 16436−16443.
(55) Joo, J.; Na, H. B.; Yu, T.; Yu, J. H.; Kim, Y. W.; Wu, F.; Zhang, J. Z.; Hyeon, T. *J. Am. Chem. Soc.* **2003**, *125*, 11100−11105.
(56) Wang, Y.; Dai, Q.; Zou, B.; Yu, W. W.; Liu, B.; Zou, G. *Langmuir* **2010**, *26*, 19129−19135.
(57) Wu, J. K.; Lyu, L. M.; Liao, C. W.; Wang, Y. N.; Huang, M. H. *Chem.−Eur. J.* **2013**, *18*, 14473−14478.
(58) Cademartiri, L.; Bertolotti, J.; Sapienza, R.; Wiersma, D. S.; Greymann, G. V.; Ozin, G. A. *J. Phys. Chem. B* **2006**, *110*, 671−673.
(59) Li, H.; Chen, D.; Li, L.; Tang, F.; Zhang, L.; Ren, J. *CrystEngComm* **2010**, *12*, 1127−1133.
(60) Wang, Z. W.; Chen, O.; Cao, C. Y.; Finkelstein, K.; Smilgies, D. M.; Lu, X.; Bassett, W. A. *Rev. Sci. Instrum.* **2010**, *81*, 093902.
(61) Wang, Z. W.; Schliehe, C.; Wang, T.; Nagaoka, Y.; Cao, Y. C.; Bassett, W. A.; Wu, H.; Fan, H.; Weller, H. *J. Am. Chem. Soc.* **2011**, *133*, 14484−14487.
(62) Suzuki, M.; Ogaki, T. *J. Am. Oil Chem. Soc.* **1985**, *62*, 1600−1604.
(63) Kanoek, F.; Yamazaki, K.; Kitagawa, K.; Kikyo, T.; Kobayashi, M.; Kitagawa, Y.; Matsuura, Y.; Sato, K.; Suzuki, M. *J. Phys. Chem. B* **1997**, *101*, 1803−1809.
(64) Sato, K. *Prog. Colloid Polym. Sci.* **1998**, *108*, 58−66.
(65) Moreels, I.; Juaro, Y.; De Geyter, B.; Haustraete, K.; Martins, J. C.; Hens, Z. *ACS Nano* **2011**, *5*, 2004−2012.
(66) Bealing, C. R.; Baumgardner, W. J.; Choi, J. J.; Hanrath, T.; Hennig, R. G. *ACS Nano* **2012**, *6*, 2118−2127.
(67) Choi, J. J.; Bealing, C. R.; Bian, K.; Hughes, K. J.; Zhang, W.; Smilgies, D. M.; Hennig, R. G.; Engstrom, J. R.; Hanrath, T. *J. Am. Chem. Soc.* **2011**, *133*, 3131−3138.
(68) Fritzinger, B.; Moreels, I.; Lommens, P.; Koole, R.; Hens, Z.; Martins, J. C. *J. Am. Chem. Soc.* **2009**, *131*, 3024−3032.
(69) Moreels, I.; Fritzinger, B.; Martines, J. C.; Hens, Z. *J. Am. Chem. Soc.* **2008**, *120*, 15081−15086.
(70) Schapotschnikow, P.; Pool, R.; Vlugt, T. J. *Nano Lett.* **2008**, *8*, 2930.
(71) Yu, L. *Acc. Chem. Res.* **2010**, *43*, 1257−1266.
(72) Nangia, A. *Acc. Chem. Res.* **2008**, *41*, 595−604.
(73) Desiraju, G. R. *J. Am. Chem. Soc.* **2013**, *135*, 9952−9967.
(74) Horie, M.; Suzaki, Y.; Hashizume, D.; Abe, T.; Wu, T.; Sassa, T.; Hosokai, T.; Osakada, K. *J. Am. Chem. Soc.* **2012**, *134*, 17932−17944.
(75) Salvalaglio, M.; Vetter, T.; Giberti, F.; Mazzotti, M.; Parrinello, M. *J. Am. Chem. Soc.* **2012**, *134*, 17221−17233.
(76) Bowden, N. B.; Weck, M.; Choi, I. S.; Whitesides, G. M. *Acc. Chem. Res.* **2001**, *34*, 231−238.
(77) Plass, K. A.; Grzesiak, A. L.; Matzger, A. J. *Acc. Chem. Res.* **2007**, *40*, 287−293.
(78) Wang, Z. W.; Wen, X. D.; Hoffmann, R.; Son, J. S.; Li, R. P.; Fang, C. C.; Smilgies, D. M.; Hyeon, T. *Proc. Natl. Acad. Sci. U.S.A.* **2010**, *107*, 17119−17124.
(79) Zeng, C.; Li, T.; Das, A.; Rosi, N. L.; J. R. C. *J. Am. Chem. Soc.* **2013**, *135*, 10011−10013.
(80) Jadzinsky, P. D.; Calero, G.; Ackerson, C. J.; Bushnell, D. A.; Kornberg, R. D. *Science* **2007**, *318*, 430−433.
(81) Yoon, B.; Luedtke, W. D.; Barnett, R. N.; Gao, J. P.; Desireddy, A.; Conn, B. E.; Bigioni, T.; Landman, U. *Nat. Mater.* **2014**, *13*, 807−811.